coatings

MDPI

Article

The Relevance of Process Parameter Optimization and Geometric Figure for Direct Laser Deposition of Inconel 738 Alloy and Its Theoretical Modeling

Kun Qi [1], Wenxing Wu [2], Pinghu Chen [1], Hao Liu [1] and Changjun Qiu [1,*]

[1] Key Laboratory of Hunan Province of Equipment Safety Service Technology under Extreme Environment, College of Mechanical Engineering, University of South China, Hengyang 421001, China; qikun18955500214@163.com (K.Q.); chenpinghu1986@163.com (P.C.); liuhao10212510@163.com (H.L.)
[2] School of Nuclear Science and Technology, University of South China, Hengyang 421001, China; wuzhiaifrank@hotmail.com
* Correspondence: qcj@usc.edu.cn

Abstract: In order to minimize the gaps between the direct laser deposition channels and improve the quality and performance of the formed parts, the process of direct laser deposition is utilized in laser additive manufacturing to create sequential, single- and double-channel deposition layers on 304 stainless steel plates. Under the premise of keeping the layer rate and defocusing amount unchanged, this study investigates the effects of laser power, scanning speed, and powder feeding rate on the morphology and inclusions of single- and double-channel deposited layers. The aim is to determine the optimal process parameter values for direct laser deposition of single-layer, single-channel Inconel 738. The effects of the three process parameters on the response values were investigated using a multi-factor, multi-level experimental design. The evaluation indexes for the analysis included the deposited layer wetting angle and aspect ratio. The analysis involved one-way extreme analysis and ANOVA analysis. The optimal process parameters are a laser power of 550~750 W, a scanning speed of 7~13 mm/s, and the powder feeding rate was 2.1~4.33 g/min. At the same time, the relationship between surface tension and gravity was integrated with the spherical coronal model and Young's equation to develop a mathematical model of the direct laser deposition process at a theoretical level. The mathematical model of the direct laser deposition process was utilized to analyze the correlation between the geometric parameters of the cross-section of the deposited layer. This analysis provides a valuable data reference for future Inconel 738 direct laser deposition.

Keywords: laser additive manufacturing; process parameter optimization; geometrical shape; theoretical derivation

check for updates

Citation: Qi, K.; Wu, W.; Chen, P.; Liu, H.; Qiu, C. The Relevance of Process Parameter Optimization and Geometric Figure for Direct Laser Deposition of Inconel 738 Alloy and Its Theoretical Modeling. *Coatings* **2023**, *13*, 1926. https://doi.org/10.3390/coatings13111926

Academic Editor: Roberto Teghil

Received: 18 October 2023
Revised: 8 November 2023
Accepted: 9 November 2023
Published: 10 November 2023

Copyright: © 2023 by the authors. Licensee MDPI, Basel, Switzerland. This article is an open access article distributed under the terms and conditions of the Creative Commons Attribution (CC BY) license (https://creativecommons.org/licenses/by/4.0/).

1. Introduction

Nowadays, it is common to investigate the effects of various process parameters on the properties of molded parts prepared using Inconel 738 laser direct deposition molding. However, the properties of the molded parts are more affected by changes in the morphology of individual passes and layers. The influence of inclusions between passes on the properties of the molded parts is even more significant under different combinations of process parameters. Currently, there are very few studies of this nature. Inconel 738 exhibits an excellent high-temperature strength, toughness, hardness, and resistance to heat corrosion, making it a popular choice for various applications, such as ships, industrial gas turbines, nuclear reactors, and petrochemicals. It is also used in high-end components, such as aeroengines and supersonic airplanes [1,2]. However, Inconel 738 faces problems with weldability and susceptibility to hot cracking, which significantly impact its machinability and the performance of its components. At present, the inclusion

cracking issue of Inconel 738 alloy can be addressed through three main approaches: optimizing the powder composition, optimizing the process parameters of laser additive manufacturing, and incorporating physical field technology. It has attracted great attention in various fields, and related research work has been carried out [3–5]. Compared to other popular alloys, such as Inconel 718, Inconel 600, Monel 400, and Ti6Al4V, Inconel 738 holds a greater economic and industrial significance. Driven by the increasing demand in recent years, the market size of nickel-based alloys has grown significantly. It is projected that the market value in 2020 will reach approximately CNY 11.096 billion. In the field of aerospace engines, the use of nickel-based alloy materials comprises from 40% to 60% of the total, with a market value of CNY 6.203 billion. In the field of nuclear power, the market is worth CNY 1.979 billion. In recent years, China has experienced a steady growth in the production of nickel-based alloys. In 2020, the output of nickel-based alloys reached approximately 27,600 metric tons, with a sales volume of about 50,900 metric tons. Among them, the use of Inconel 738 has surpassed one-third of the total utilization of nickel-based alloys. With the continuous growth of the downstream nickel-based alloy industry, the industry scale is also projected to expand in the future. It is expected that the industry value will reach CNY 55.034 billion by 2027.

Laser additive manufacturing (LAM) can create a three-dimensional model of the metal parts by using professional software to slice and layer the data, resulting in a two-dimensional deposition path. Through the use of digital technology, a high-energy laser beam will be employed to achieve the direct formation of three-dimensional parts with a high degree of freedom. This will be accomplished by melting and depositing the material point by point, line by line, and surface by surface [6,7]. Direct laser deposition (DLD) is based on the principle of discrete/stacking by layering the 3D CAD model of the part, obtaining the 2D contour information of each layer's cross-section, and generating the machining path. In an inert gas-protected environment, high-energy-density lasers are used as the heat source to melt and stack powders or wires layer by layer along a predetermined machining path. This process enables the direct manufacturing and repair of metal parts. The most effective approach to address the issues of poor forming and cracking in the manufacturing of Inconel 738 using direct laser deposition technology is to optimize the parameters of the forming process. The change in process parameters will directly affect the deposition geometry, microstructure, residual stress, and mechanical properties. Therefore, it is necessary to conduct relevant studies on the process parameters in order to obtain dense and high-performance depositions [8]. The selection of process parameters, such as the laser power, scanning speed, and powder feeding rate, plays a crucial role in the quality of the mold [9]. The deposition gradually transitions from a single to multiple coats, and the quality of the single coat directly affects the overall quality [10,11]. Quality assessment requires a defect-free surface, without cracks, with appropriate values for the height, width, height-to-width ratio, and wetting angle size. In recent years, numerous scholars have developed models and empirical formulas to examine the impact of process parameters and their combinations on deposition morphology and properties. This has been achieved through the use of response surface analysis and linear regression analysis [12]. Perevoshchikova et al. [13] achieved a microcrack-free and macroscopic porosity of only 0.5% in molded samples by using a low-energy laser, setting a medium scanning speed, and employing a small scanning pitch. The interaction among scanning speed, laser power, and scanning spacing greatly influences the formation of microcracks and pores. Mondal et al. utilized the width and depth of the deposition as indicators to investigate the impact of each process parameter on deposition. This was achieved through the implementation of an orthogonal experimental design, an artificial neural network, and analysis of variance [14]. Barekat et al. investigated the relationship between the laser power, scanning speed, powder feed rate, and the geometrical characteristics of single-layer, single-pass depositions. They conducted a linear regression analysis and designed a guide for selecting the process parameters to achieve the desired deposition characteristics [15]. Ansari [16] proposed the use of a regression model to predict the deposition morphology.

This was achieved by analyzing the effect of laser additive manufacturing parameters on the deposition morphology using nickel-based alloy powder. T. Muthuramalingam [17] utilized the Taguchi–Grey correlation method to examine the impact of process parameters on surface property measurements while machining titanium alloys. It was found that the laser power (3 kW), nozzle distance (1.5 mm), focal length (−2 mm), and gas pressure (2 bar) were determined to be the optimal combinations of process parameters, resulting in less plasma energy and an accuracy of 2.2%. Ammar H. Elsheikh [18] conducted statistical analysis to examine the impact of various laser cutting parameters on the kerf characteristics. The results showed that increasing in cutting parameters leads to an increase in the top and bottom width of the saw kerf, while increasing in cutting speed or laser power leads to an increase in the taper of the kerf. Ahmed B. Khoshaim [19] utilized the Taguchi L18 hybrid design to investigate the impact of four process parameters (laser power, cutting speed, auxiliary gas pressure, and plate thickness) on five process responses: the kerf deviation, top heat-affected zone, bottom heat-affected zone, maximum surface roughness, and roughness area. The results show that as the laser power increases, the cutting speed decreases, the surface roughness worsens, and the heat-affected zone widens. Ammar H. Elsheikh [20] proposed a solution to address the margin problem in order to accurately calculate the transient temperature field during laser heating. The experiments were conducted using a continuous-wave CO_2 laser with a maximum power of 150 W to validate the findings. Ammar H. Elsheikh [21] utilized the Taguchi L18 orthogonal array design to examine the impact of four input variables—gas pressure, sheet thickness, laser power, and cutting speed—on five kerf quality metrics: the rough zone ratio, upper and lower heat-affected zone width, maximum surface roughness, and kerf taper angle. The results show that the RVFLEO model has a strong ability to accurately predict the laser-cutting characteristics of PMMA sheets.

In this paper, a multi-factorial and multi-level experimental design was adopted to investigate the effects of changes in the process parameters on the morphology of the deposited layer and the inclusions between channels. This was achieved through one-way analysis, extreme analysis, and analysis of variance (ANOVA) using three process parameters: the laser power, scanning speed, and powder feeding rate, as the influencing factors. The responses measured were the wetting angle, height, width, and their ratios. The goal was to determine the optimal values of the process parameters that would result in the lowest number of inclusions in the multi-channel deposited layer. The optimal value for each process parameter is obtained when there is a minimum of multi-channel sedimentary layer inclusions. At the same time, a mathematical model was developed to characterize the relationship between the geometrical parameters of the cross-section and the surface tension and gravity. This was conducted in conjunction with the theoretical derivation of the spherical crown model.

2. Experimental

2.1. Experimental Equipment and Materials

In this experiment, the coaxial powder feeding method is utilized for laser material deposition on the substrate surface. The laser material deposition platform equipment comprises an XL-1000 laser, an HW-05SF powder feeder, a CWFL-1000 refrigeration controller, a CW-5000 water-cooling system, and a 4-axis CNC6090 numerical control platform. The laser's rated power is 1000 W, and argon is used as both the protective gas and the carrier gas.

The substrate used for the experiment is 304 stainless steel, and the forming material is Inconel 738 alloy powder. The chemical composition (mass fraction) is shown in Table 1.

Table 1. Mass fractions of chemical elements in 304 stainless steel and Inconel 738 alloy powder.

Material	Chemical Composition (%)								
	C	Si	Mn	Cr	Co	S	P	N	Al
304	≤0.08	≤1.0	≤2.0	18.0~20.0	-	≤0.03	≤0.035	≤0.1	-
Inconel 738	0.095	-	-	15.88	8.66	-	-	-	3.51
	Mo	Nb	Ta	Ti	W	Zr	B	Fe	Ni
304	-	-	-	-	-	-	-	Bal	8.0~10.5
Inconel 738	1.76	0.86	1.76	3.49	2.65	0.022	0.009	0.09	Bal

The comparison of the properties of Inconel 738 with other popular alloys, namely Inconel 718, Inconel 600, Monel 400, and Ti6Al4V, is shown in Table 2 below.

Table 2. Comparison of the properties of Inconel 738 with other superalloys.

Capability / Materials	Inconel 738	Inconel 718	Inconel 600	Monel 400	Ti6Al4V
Density	8.11 kg/dm^3	8.22 kg/dm^3	8.4 kg/dm^3	8.83 kg/dm^3	2.5 kg/dm^3
Hardness	41–43 HR	23–46 HR	65 HR	60–96 HR	25–40 HR
Strength	Yield strength: 951 MPa Tensile strength: 1096 MPa	Yield strength: 317.2–1300 MPa Tensile strength: 800–1950 MPa	Yield strength: ≥245 MPa Tensile strength: ≥550 MPa	Yield strength: 172–1104 MPa Tensile strength: 400–1100 MPa	Yield strength: 827–1034 MPa Tensile strength: ≥896 MPa
Ductility	5.5%	3%–42%	≥30%	2%–50%	≥3%
Fatigue life	124 Mpa	3950 MPa	283 MPa	279 MPa	1619 MPa
Thermal conductivity	13–84 W/(m °C)	10.9–11.4 W/(m·°C)	12.4–14.4 W/(m·°C)	21.8 W/(m·°C)	7.04–7.23 W/(m·°C)
Thermal expansion coefficient	12.87–15.93 × 10^{-6}/°C	2.14–12.31 × 10^{-6}/°C	11.69–11.89 × 10^{-6}/°C	13.8 × 10^{-6}/°C	8.68–8.75 × 10^{-6}/°C

2.2. Experimental Methods

Before the experiment, the surface of the substrate was polished successively with a grinder and sandpaper. It was then cleaned with ethanol and acetone to remove any surface grease and stains. The substrate was subsequently dried in a drying oven, along with the powder for 2 h. After the experiment, the substrate was cooled to room temperature, and long-strip specimens were cut along the direction perpendicular to the fusion sediment. Then, each group of long strip specimens was cut into small samples, and the small samples were mounted and polished using 180–2000 grit sandpaper. This process allowed the creation of a cross-section of the deposited layer, as depicted in Figure 1. The height H and width W of the deposit layer were photographed and measured using an optical imager. The pictures were then imported into AutoCAD to measure the wetting angle. The cross-section of the deposit layer and the geometric dimensions are shown in Figure 2.

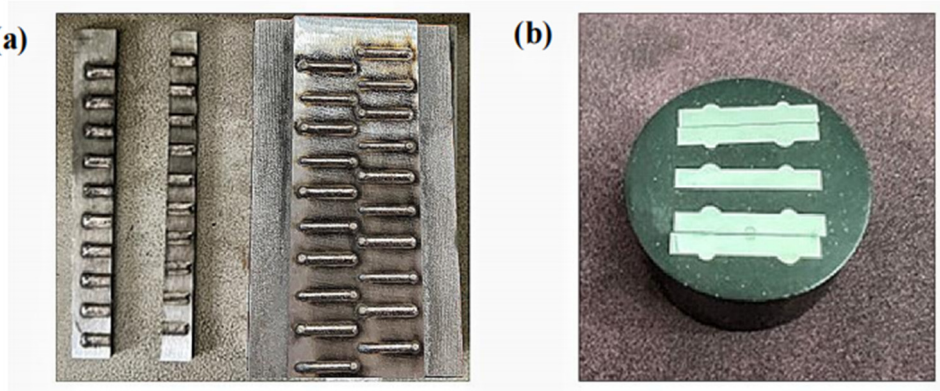


Figure 1. (**a**) Macrographs of the surfaces of single- and double-pass deposited layers using direct laser deposition, as well as a long-cut specimen. (**b**) Macroscopic view of the cross-section of a long specimen after wire cutting and mounting.

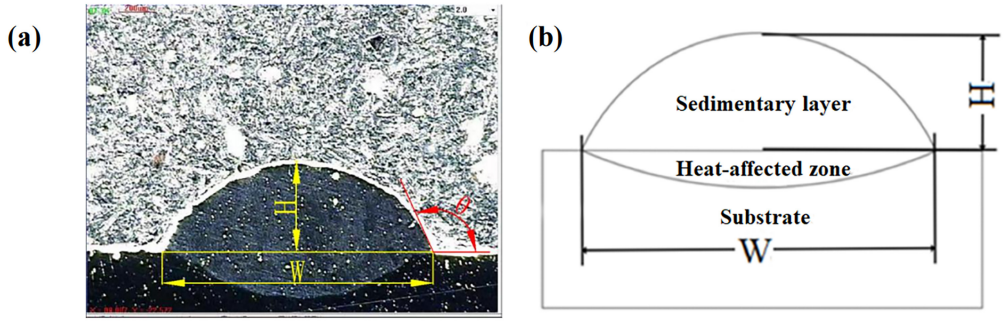


Figure 2. (**a**) Cross-sectional morphology of a single-layer, single-pass object formed through laser direct deposition. (**b**) Theoretical cross-sectional morphology of single-layer, single-pass laser direct deposition molding.

Figure 1a shows the laser deposition on the substrate, which is directly formed by a single layer of a single-channel, macro-photomorphological map and its wire-cut, long specimens. Figure 1b was obtained from Figure 1a based on the long specimens, which can be used for paneling. Figure 1b shows the macro-photomorphological map of the cross-section after paneling. Figure 2a depicts a microscopic cross-sectional geometrical profile of a single-channel deposition layer captured using an optical imager. In contrast, Figure 2b illustrates a theoretical cross-sectional profile of a single-channel deposition layer created using CAD.

3. Experimental Results and Analysis

Based on the multi-factorial and multi-level experimental design, five levels of laser power, four levels of scanning speed, and three levels of powder feeding rate were selected. The width of the deposited layer W, the height H, the aspect ratio H/W, and the wetting angle θ were used as the four response variables.

The results of the experimental design are shown in Table 3 and Figures 3 and 4.

Table 3. Multi-factor and multi-level experimental design scheme and results.

Depots	Laser Power P/W	Scanning Speed Vs/(mm/s)	Powder Feeding Rate Vf/(g/min)	Welding Width W/mm	Welding Height H/mm	Ratio of Deposition Height to Deposition Width H/W	Wetting Angle of Deposition Layer θ/°
1	550	7	6.67	1.495	0.996	0.666	81.50
2	600	7	6.67	1.561	0.827	0.530	90.00
3	650	7	6.67	1.705	0.884	0.518	85.06
4	700	7	6.67	1.825	0.971	0.532	94.61
5	750	7	6.67	1.803	1.065	0.591	72.51
6	550	9	6.67	1.478	0.636	0.430	105.38
7	600	9	6.67	1.582	0.759	0.480	103.53
8	650	9	6.67	1.666	0.728	0.437	107.93
9	700	9	6.67	1.700	0.763	0.449	77.29
10	750	9	6.67	1.763	0.785	0.445	101.22
11	550	11	6.67	1.395	0.532	0.381	85.13
12	600	11	6.67	1.495	0.609	0.407	104.77
13	650	11	6.67	1.589	0.664	0.418	110.05
14	700	11	6.67	1.665	0.725	0.435	96.97
15	750	11	6.67	1.750	0.698	0.399	118.13
16	550	13	6.67	1.502	0.617	0.411	116.94
17	600	13	6.67	1.481	0.564	0.381	116.32
18	650	13	6.67	1.522	0.503	0.330	118.26
19	700	13	6.67	1.666	0.557	0.334	119.47
20	750	13	6.67	1.726	0.606	0.351	120.56
21	550	7	4.33	1.666	0.616	0.370	100.96
22	600	7	4.33	1.766	0.652	0.369	114.87
23	650	7	4.33	1.809	0.611	0.338	101.80

Table 3. *Cont.*

Depots	Laser Power P/W	Scanning Speed Vs/(mm/s)	Powder Feeding Rate Vf/(g/min)	Welding Width W/mm	Welding Height H/mm	Ratio of Deposition Height to Deposition Width H/W	Wetting Angle of Deposition Layer θ/°
24	700	7	4.33	1.927	0.654	0.339	113.11
25	750	7	4.33	1.920	0.676	0.352	99.28
26	550	9	4.33	1.431	0.521	0.364	116.18
27	600	9	4.33	1.629	0.541	0.332	120.96
28	650	9	4.33	1.692	0.649	0.384	119.02
29	700	9	4.33	1.734	0.637	0.367	112.93
30	750	9	4.33	1.797	0.618	0.344	115.37
31	550	11	4.33	1.413	0.589	0.417	105.85
32	600	11	4.33	1.502	0.583	0.388	111.36
33	650	11	4.33	1.603	0.493	0.308	121.13
34	700	11	4.33	1.659	0.598	0.360	112.59
35	750	11	4.33	1.703	0.538	0.316	108.98
36	550	13	4.33	1.384	0.358	0.258	117.55
37	600	13	4.33	1.510	0.384	0.254	128.31
38	650	13	4.33	1.532	0.424	0.277	118.13
39	700	13	4.33	1.623	0.476	0.293	124.48
40	750	13	4.33	1.715	0.495	0.289	128.14
41	550	7	2.1	1.629	0.553	0.339	116.34
42	600	7	2.1	1.710	0.549	0.322	106.60
43	650	7	2.1	1.817	0.536	0.295	127.67
44	700	7	2.1	1.854	0.498	0.269	123.53
45	750	7	2.1	1.904	0.470	0.247	132.36
46	550	9	2.1	1.494	0.412	0.276	122.12
47	600	9	2.1	1.581	0.432	0.273	133.36
48	650	9	2.1	1.610	0.444	0.276	118.60
49	700	9	2.1	1.700	0.522	0.307	120.46
50	750	9	2.1	1.780	0.460	0.259	124.04
51	550	11	2.1	1.452	0.347	0.239	129.27
52	600	11	2.1	1.547	0.322	0.208	132.94
53	650	11	2.1	1.615	0.335	0.207	129.92
54	700	11	2.1	1.817	0.367	0.202	133.90
55	750	11	2.1	1.868	0.378	0.202	139.60
56	550	13	2.1	1.472	0.286	0.194	148.21
57	600	13	2.1	1.484	0.283	0.191	135.64
58	650	13	2.1	1.555	0.251	0.161	135.54
59	700	13	2.1	1.606	0.252	0.157	142.18
60	750	13	2.1	1.671	0.237	0.142	135.57

As shown in Figures 3 and 4, 60 sets of single-layer, single-pass, single-layer multi-pass, and single-layer, single-pass theoretical cross-sections are demonstrated at laser powers of 550 W, 600 W, 650 W, 700 W, and 750 W; scanning speeds of 7 mm/s, 9 mm/s, 11 mm/s, and 13 mm/s; and powder feeding rates of 2.1 g/min, 4.33 g/min, and 6.67 g/min. The single-layer, single-pass theoretical cross-sections were drawn using Shapr3D software (Version number: 3.46.1). Table 2 displays the 60 groups of single-layer, single-pass physical cross-sections, along with the corresponding height and width measurements obtained using the optical imager. By using Shapr3D software, the height and width of each physical cross-section were sequentially defined. This allows the creation of a theoretical single-layer, single-channel cross-section. In this case, each group of process parameter combination experiments was repeated three times, which ensures the sufficient reproducibility and high accuracy of the obtained data.

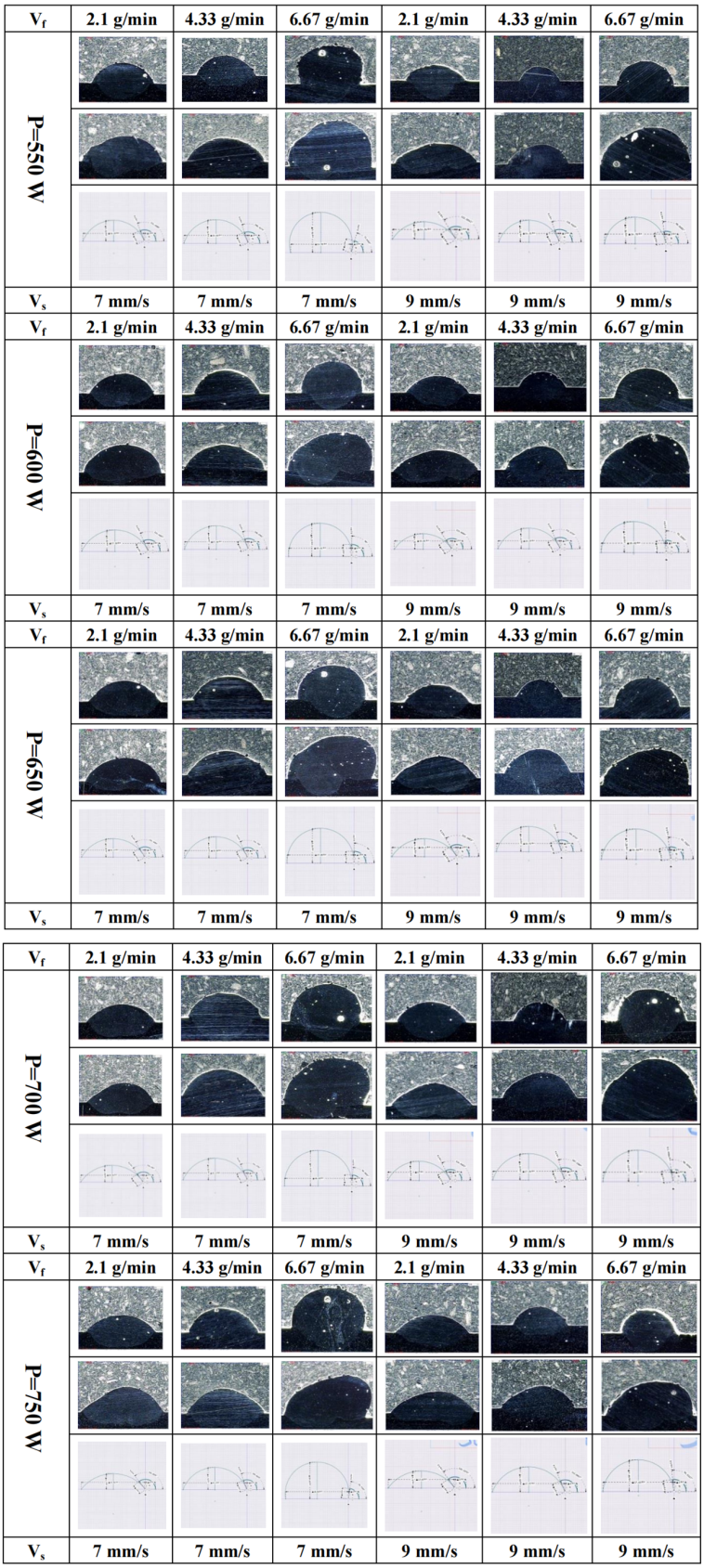


Figure 3. At scanning speeds of 7 mm/s and 9 mm/s, different process parameters are combined with single-channel, double-channel, and single-channel theoretical cross-section morphologies.

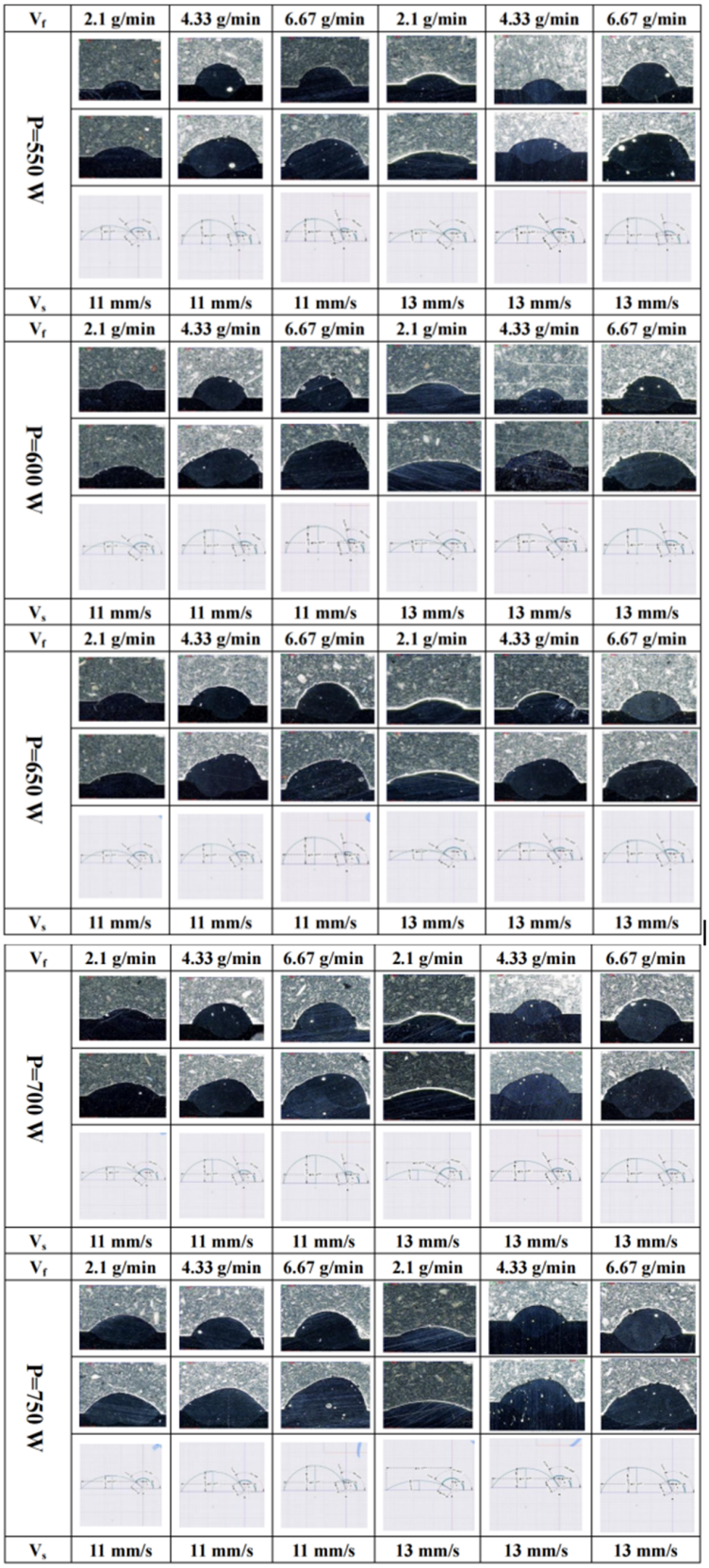


Figure 4. At scanning speeds of 11 mm/s and 13 mm/s, different process parameters are combined with single-channel, double-channel, and single-channel theoretical cross-section morphologies.

3.1. One-Way Analysis of Variance

(1) *The widths of the depositions*

We used Origin 2018 to plot the trend curve for the width of the layer deposited via laser power. As shown in Figure 5, the width of the deposited layer exhibits an increasing trend with the rise in laser power, assuming all the other conditions remain constant. This is because as the laser power increases, it primarily impacts two factors. Firstly, the energy input to the substrate's surface increases, leading to an expansion in the size of the molten pool. Consequently, the width of the molten pool also increases. Secondly, the quantity of laser-melted metal powder increases, resulting in a larger amount of material involved in the formation of the deposited layer. This, in turn, contributes to a wider width. The scanning speed has a negative effect on width, and increasing the scanning speed will, to some extent, cause the width to decrease. This is because a scanning speed that is too fast reduces the amount of linear energy input per unit length.

(2) *The heights of the depositions:*

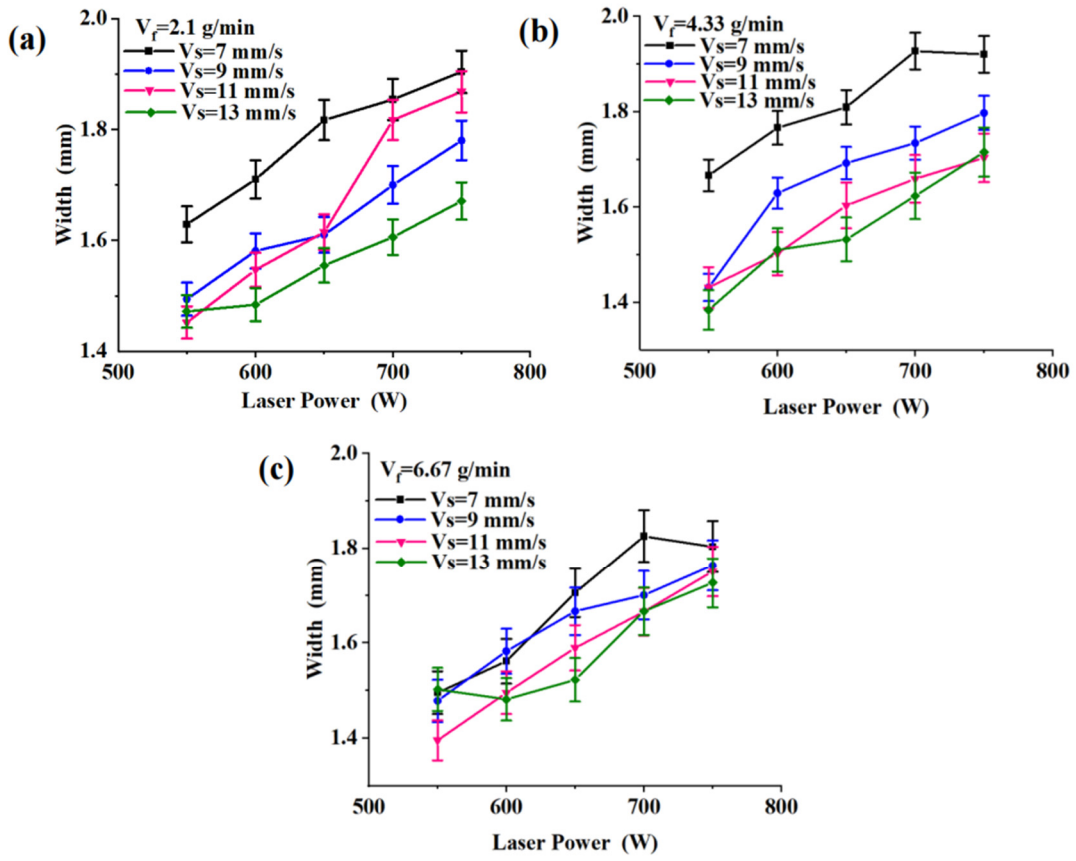


Figure 5. Effect of laser power on widths of the depositions. (**a**) V_f = 2.1 g/min, (**b**) V_f = 4.33 g/min, and (**c**) V_f = 6.67 g/min.

As can be seen in Figures 6 and 7, the height of the deposited layer decreases with an increase in the scanning speed and increases with an increase in the powder delivery rate, while keeping the other parameters constant. The reason for this phenomenon can be explained as follows: The increase in scanning speed causes the laser to spend less time at a specific position on the substrate. This leads to a decrease in the amount of energy applied per unit length, resulting in a reduction of melted metal powder and a smaller or shallower molten pool. Secondly, under the premise of maintaining a constant powder feeding rate, increasing the scanning speed will result in a decrease in the mass flow rate per unit length of the powder. The increase in the powder feed rate results in a higher amount of powder that can be melted

by the laser per unit of time. This, in turn, leads to a greater amount of powder being involved in the formation of the deposition layer, resulting in an increase in height.

(3) *The wetting angles of the depositions:*

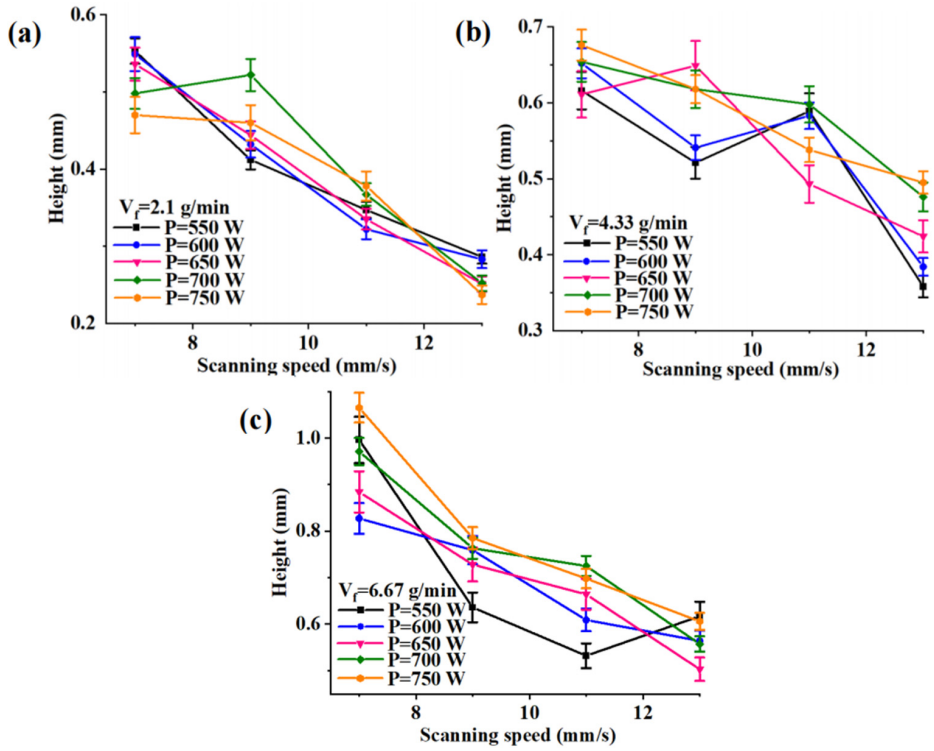


Figure 6. Effect of scanning speed on heights of the depositions. (**a**) V_f = 2.1 g/min, (**b**) V_f = 4.33 g/min, and (**c**) V_f = 6.67 g/min.

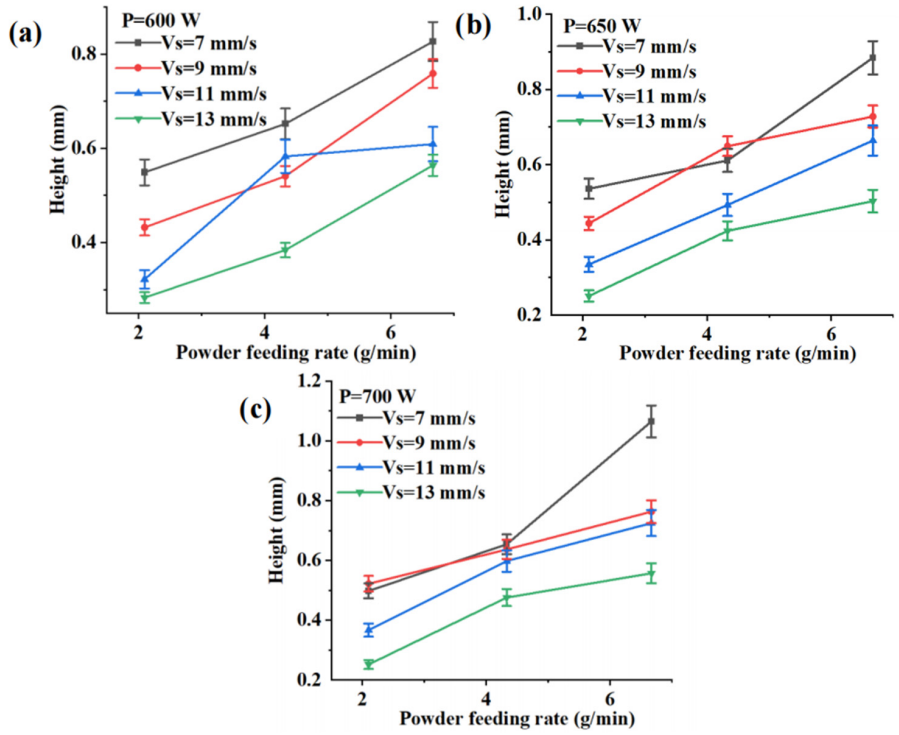


Figure 7. Effect of powder feeding rate on heights of the depositions. (**a**) V_f = 2.1 g/min, (**b**) V_f = 4.33 g/min, and (**c**) V_f = 6.67 g/min.

From Figure 8, it can be observed that the wetting angle gradually decreases as the powder feeding rate increases, while keeping the laser power and scanning speed constant. This can be attributed to the previous variations in height. From Figure 7, it can be observed that when other parameters are held constant, an increase in the powder feeding rate leads to a gradual increase in height. Consequently, the wetting angle becomes steeper and smaller. With the increase in scanning speed, the wetting angle gradually becomes larger. This is because the increase in scanning speed leads to a decrease in height, resulting in a larger wetting angle. As shown in the figure, when the laser power is increased to over 650 W, the wetting angle formed at a scanning speed of 7 mm/s is greater than the angle formed at 9 mm/s, while the powder feeding rate remains at 2.1 g/min. This indicates that, under this specific combination of parameters, the excessively high power level leads to a sudden alteration in the formation of the wetting angle.

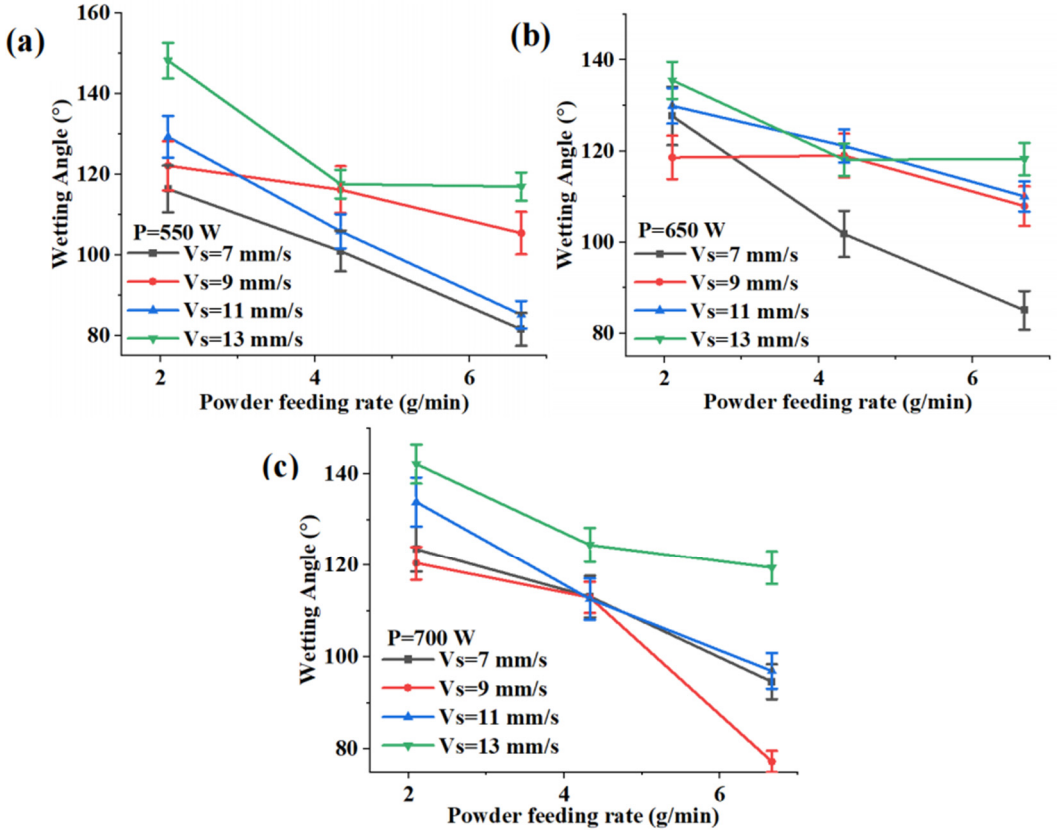


Figure 8. Effect of powder feeding rate on wetting angle of the depositions. (**a**) P = 550 W, (**b**) P = 650 W, and (**c**) P = 700 W.

3.2. Extreme Analysis

Based on the 60 groups of multi-factorial and multi-level experimental data in Table 4, single-factor analysis was conducted to determine the impact of each group of process parameter combinations on the geometrical shape of the fused deposition layer. Therefore, based on single-factor analysis, it is important to select representative combinations of process parameters for orthogonal experimental extreme analysis. Using the wetting angle as the reference index, the data results were obtained from 23 groups of parameter combinations with a single-pass wetting angle greater than 120°. These results were selected from a total of 60 groups of process parameter combinations. The laser power values of 600 W, 650 W, and 700 W; scanning speeds of 9 mm/s, 11 mm/s, and 13 mm/s; and powder feeding rates of 2.1 g/min, 4.33 g/min, and 6.67 g/min were analyzed using polar analysis and an orthogonal experimental design. The analysis aimed to determine the primary and secondary orders of influence for each factor. An orthogonal experimental design was

used for polar analysis to determine the primary and secondary orders of influence of each factor. According to the calculation rule of the orthogonal experiment, the results of the orthogonal experiment with three factors and three levels were calculated and are listed in Table 4.

Table 4. Orthogonal experiment scheme and result analysis.

Test Pieces	Laser Power P/W	Scanning Speed Vs/(mm/s)	Powder Feeding Rate Vf/(g/min)	Welding Width W/mm	Welding Height H/mm	Wetting Angle of Deposition Layer θ/°	Ratio of Deposition Height to Deposition Width H/W
1	600	9	2.1	1.581	0.432	133.359	0.273
2	600	11	4.33	1.502	0.583	111.360	0.388
3	600	13	6.67	1.481	0.564	116.316	0.381
4	650	9	4.33	1.692	0.649	119.020	0.384
5	650	11	6.67	1.589	0.664	110.052	0.418
6	650	13	2.1	1.555	0.251	135.535	0.161
7	700	9	6.67	1.700	0.763	77.287	0.449
8	700	11	2.1	1.817	0.367	133.902	0.202
9	700	13	4.33	1.623	0.476	124.480	0.293
KW1	1.521	1.658	1.651	-	-	-	-
KW2	1.612	1.636	1.606	-	-	-	-
KW3	1.713	1.553	1.590	-	-	-	-
Range RW	0.192	0.105	0.061	-	-	-	-
KH1	0.526	0.615	0.350	-	-	-	-
KH2	0.521	0.538	0.569	-	-	-	-
KH3	0.535	0.430	0.664	-	-	-	-
Range RH	0.014	0.185	0.314	-	-	-	-
Kθ1	120.345	109.889	134.265	-	-	-	-
Kθ2	121.536	118.438	118.287	-	-	-	-
Kθ3	111.890	125.444	101.218	-	-	-	-
Range Rθ	9.646	15.555	33.047	-	-	-	-

In Table 4, K1, K2, and K3 represent the average values of the three levels of the respective indicators in the columns where the factors are located. R represents the calculated range, and the subscripts W, H, and θ represent the values associated with the width, height, and wetting angle of the fused deposition layer, respectively.

From Table 4, it can be observed that RW (P) > RW (V_S) > RW (V_f), RH (V_f) > RH (V_S) > RH (P), and Rθ (V_f) > Rθ (V_S) > Rθ (P). This indicates that the deposition width is primarily influenced by the laser power, followed by the scanning speed, and lastly, the powder feeding rate. On the other hand, both the deposition height and the wetting angle are mainly affected by the powder feeding rate, followed by the scanning speed, and finally the laser power.

According to the results of orthogonal experiments, Mini Tab software (The version number: 21) was used to analyze the height of the deposition layer H, width W, aspect ratio H/W, and wetting angle θ as the response indices for data processing. The order of the influence of each factor on the response indices as well as the trend of change were determined using the mean value response table (in which the levels of A, B, and C represent the laser power, scanning speed, and powder feeding rate, respectively). The design is summarized in Table 5, and the mean response tables for the four responses are shown in Tables 6–9.

Table 5. Design summary.

Taguchi	L9 (3^3)
Factors	3
Number of experiments	9
Columns of the L9 (3^4) array	1 2 3

Table 6. The heights of the depositions mean response table.

Levels	A	B	C
1	0.5263	0.6147	0.3500
2	0.5213	0.5380	0.5693
3	0.5353	0.4303	0.3137
Delta	0.0140	0.1843	0.3137
Ordered list	3	2	1

Table 7. The widths of the depositions mean response table.

Levels	A	B	C
1	1.521	1.658	1.651
2	1.612	1.636	1.606
3	1.713	1.553	1.590
Delta	0.192	0.105	0.061
Ordered list	1	2	3

Table 8. Aspect ratio mean response table.

Levels	A	B	C
1	0.3473	0.3687	0.2120
2	0.3210	0.3360	0.3550
3	0.3147	0.2783	0.4160
Delta	0.0327	0.0903	0.2040
Ordered list	3	2	1

Table 9. Wetting angles mean response table.

Levels	A	B	C
1	120.3	109.9	134.3
2	121.5	118.4	118.3
3	111.9	125.4	101.2
Delta	9.6	15.6	33.0
Ordered list	3	2	1

As can be seen from the mean response tables in Tables 6–9, the results obtained from processing the data through Mini Tab are consistent with the experimental results calculated in Table 4. This indicates that the experimental calculations are reasonable.

From the orthogonal experiments, it can be seen that the deposition inclusions and morphology are determined jointly by various process parameters. Therefore, when selecting process parameters, it is important to consider different parameters for deposition inclusions and the morphology they cause due to their distinct effects. Based on this, ANOVA will be performed to investigate the effect of the interaction between the two factors on the deposition inclusions and morphology.

3.3. ANOVA (Analysis of Variance)

3.3.1. Influence of Process Parameters on Heights of the Depositions

It is important to control the height in order to obtain a homogeneous sediment layer. Therefore, it is important to study the effect of each factor on height and determine the percentage contributed by each factor. ANOVA was used to analyze the effect of the height of the sedimentary layer in relation to each factor, and the results are presented in Table 10.

Table 10. Results of variance analysis of heights of the depositions.

Source	DF	Adj SS	Adj MS	F	*p*
Mold	35	1.86943	0.053412	19.58	0.000
Biometrics	9	1.75167	0.194630	71.36	0.000
Laser power	4	0.02786	0.006964	2.55	0.065
Scanning speed	3	0.64929	0.216429	79.36	0.000
Powder feeding rate	2	1.07452	0.537262	196.99	0.000
2 Factor interactions	26	0.11776	0.004529	1.66	0.108
Laser power * Scanning speed	12	0.02250	0.001875	0.69	0.747
Laser power * Powder feeding rate	8	0.01915	0.002394	0.88	0.549
Scanning speed * Powder feeding rate	6	0.07610	0.012684	4.65	0.003
Error	24	0.06546	0.002727		
Total	59	1.93488			

S = 0.0522235; R-sq = 96.62%; R-sq (adj) = 91.68%; R-sq (pre) = 78.86%.

From Table 10, the F value of the model is 19.58, with a *p*-value < 0.0001, indicating that the model is statistically significant. The regression model explains 96.62% of the variation in the coating height, as shown by the regression coefficient R-sq in Table 10. The value of R-sq in this model is also very close to unity, which indicates that the adopted DOE model explains the relationship between height and the other factors well. The *p* value for the scanning speed, powder delivery rate, and their interaction is less than 0.05. Therefore, statistically, the scanning speed and powder delivery rate have the most significant impact on height. The *p* value for laser power was found to be 0.065, indicating that its impact on height was not statistically significant.

To determine the proportional effect of each factor, pie charts were created using the sum of the squares from the ANOVA table, as depicted in Figure 9a, and Pareto charts, as illustrated in Figure 9b.

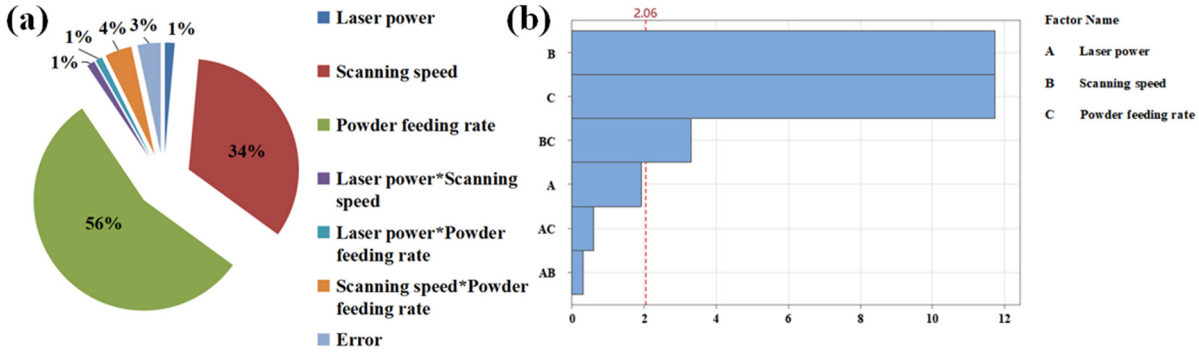


Figure 9. (**a**) Pie chart of practical significance factor of height of the depositions. (**b**) Pareto diagram in response to a height H/mm normalization effect.

As shown in Figure 9a, the powder feeding rate is responsible for 56% of the variation in height, making it the most significant parameter affecting the height. The scanning speed accounts for 34% of the variation, making it the second most important parameter. The laser power, on the other hand, only contributes to 1% of the variation in the height of the deposited layer. Figure 9b also indicates that the scanning speed, powder feeding rate, and their interaction have the most significant impact on the height, which aligns with the findings presented in Table 9 and Figure 9a.

The main effect plots and interaction plots of the main study parameters on height are shown in Figures 10 and 11, respectively.

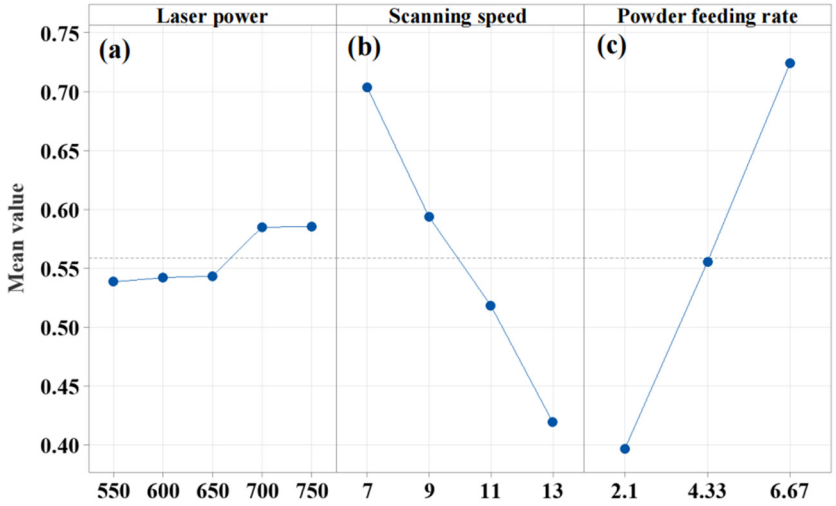


Figure 10. The response is a height H/mm main effect diagram. (**a**) Laser power. (**b**) Scanning speed. (**c**) Powder feeding rate.

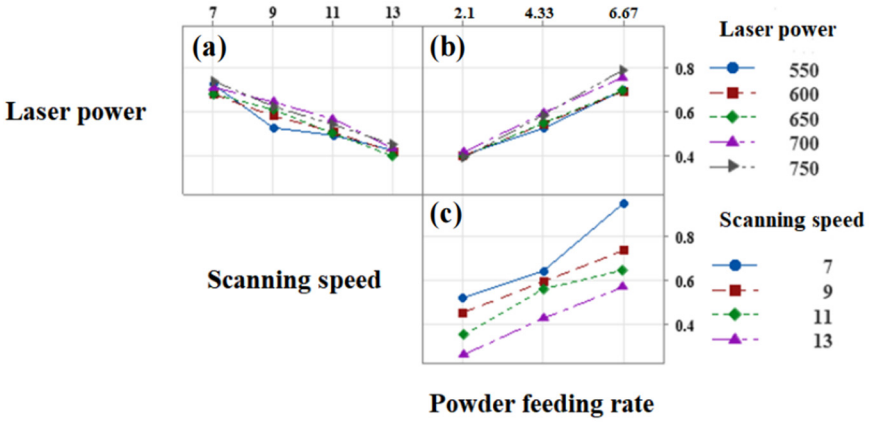


Figure 11. The response is a height H/mm interaction graph. (**a**) Laser power and scanning speed. (**b**) Laser power and powder feeding rate. (**c**) Scanning speed and powder feeding rate.

From the main effect plot, it can be observed that the maximum impact on the height of the deposited layer was achieved when the laser power was set at 750 W, the scanning speed was set at 7 mm/s, and the powder feeding rate was maintained at 6.67 g/min. And the effect on the height is much greater than the mean value level when the powder feeding rate is 6.67 g/min, followed by the scanning speed, and finally, the laser power. The change in laser power has no significant effect on the height. In fact, the heights remain almost the same at 550 W, 600 W, 650 W, 700 W, and 750 W. The heights of the layers at 550 W, 600 W, 650 W, 700 W, and 750 W are almost the same. This phenomenon can be explained by the fact that as the laser power increases, the amount of energy input also increases, resulting in a larger melt pool. However, the growth rate of the deposited layer will no longer increase significantly when the powder feed rate is maintained at a constant level. Therefore, it is also necessary to control the domain value of the laser power; otherwise, it will result in some degree of wastage. From the interaction plot, it can be seen that there is no significant interaction between the laser power and scanning speed. This is because the trend of height change is consistent with the increase in scanning speed at various laser powers. Similarly, there is no interaction between laser power and powder feeding rate.

3.3.2. Influence of Process Parameters on Widths of the Depositions

The width of the single-pass deposition layer is an important factor that affects its forming efficiency. As indicated by the regression coefficient R-Sq, the model accurately

represents 97.51 percent of the width variance, demonstrating a strong fit. This is evident in Table 11.

Table 11. Results of variance analysis of widths of the depositions.

Source	DF	Adj SS	Adj MS	F	*p*
Mold	35	1.12756	0.032216	26.85	0.000
Biometrics	9	1.03346	0.114829	95.71	0.000
Laser power	4	0.69514	0.173786	144.86	0.000
Scanning speed	3	0.32040	0.106799	89.02	0.000
Powder feeding rate	2	0.01792	0.008961	7.47	0.003
2 Factor interactions	26	0.09410	0.003619	3.02	0.004
Laser power * Scanning speed	12	0.02595	0.002162	1.80	0.106
Laser power * Powder feeding rate	8	0.00688	0.000861	0.72	0.674
Scanning speed * Powder feeding rate	6	0.06126	0.010210	8.51	0.000
Error	24	0.02879	0.001200		
Total	59	1.15635			

S = 0.0346367; R-sq = 97.51%; R-sq (adj) = 93.88%; R-sq (pre) = 84.44%.

As shown in Table 11, the model has an F value of 26.85, with a p value < 0.0001, indicating its statistical significance. Additionally, the R-Sq value is close to unity, suggesting that the DOE model accurately represents the relationship between the widths and each parameter. The standard error of the model was only 0.03, indicating that the model is accurate. The analysis results of the p values indicate that the laser power, scanning speed, powder feeding rate, and the interaction between scanning speed and powder feeding rate all have statistically significant effects on width, with values less than 0.05. The sum of squares values of the individual factors in the ANOVA table were used to determine the ratio effect of the influencing factors on width. Pie charts illustrating the practical significant factors for width were constructed, as depicted in Figure 12a, and Pareto charts are shown in Figure 12b.

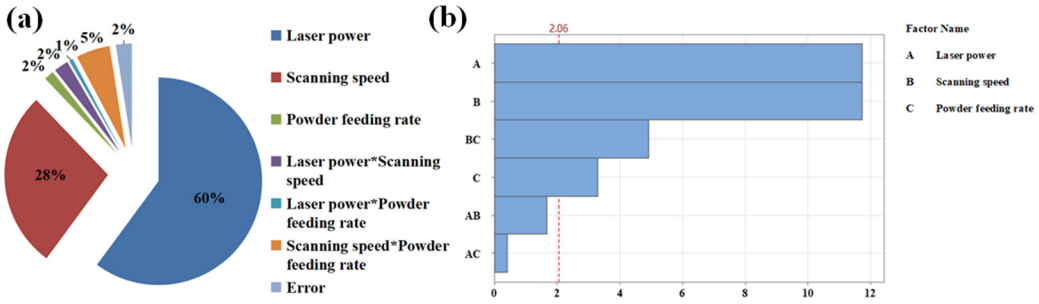


Figure 12. (**a**) Pie chart of practical significance factor of width of the depositions. (**b**) Pareto diagram in response to a width W/mm normalization effect.

As can be seen from Figure 12a, the laser power affects the width by 60% and is the most significant factor in determining the width. The scanning speed is the second most important factor, accounting for 28%. Among all the factors, only 2% of the variation is caused by the powder feeding rate. The Pareto chart also demonstrates that the laser power, scanning speed, and the interaction of the scanning speed and powder feed rate have the greatest influence on width.

The main effect plots and interaction plots of the main study parameters on width are shown in Figures 13 and 14, respectively.

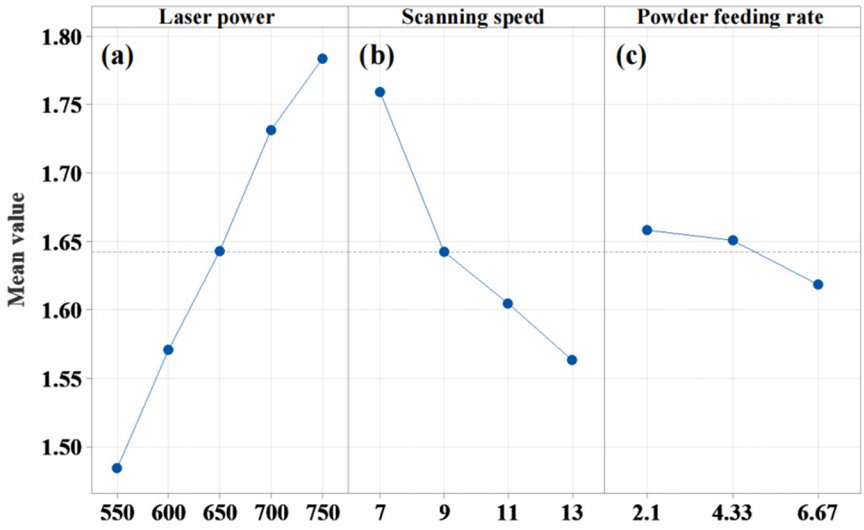


Figure 13. The response is a width W/mm main effect diagram. (**a**) Laser power. (**b**) Scanning speed. (**c**) Powder feeding rate.

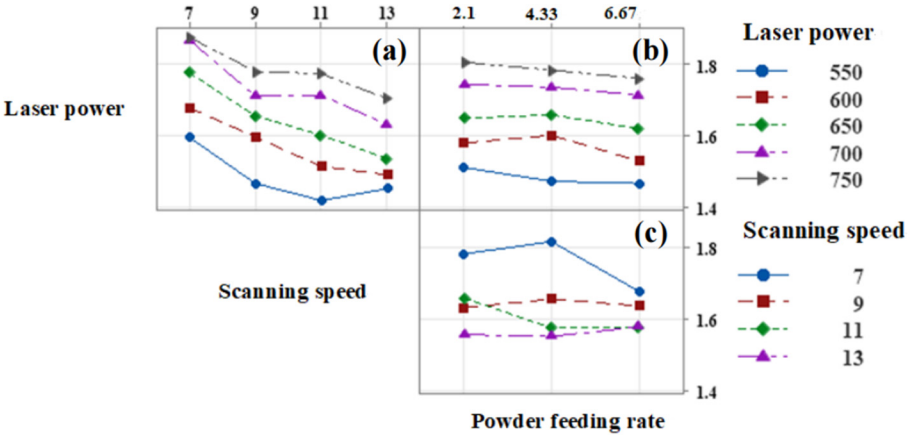


Figure 14. The response is a width W/mm interaction graph. (**a**) Laser power and scanning speed. (**b**) Laser power and powder feeding rate. (**c**) Scanning speed and powder feeding rate.

From Figure 13, it can be seen that the width of the deposited layer is most affected when the laser power is set to 750 W, the scanning speed is 7 mm/s, and the powder feeding rate is 2.1 g/min. The effect on the width is much greater than the mean value when the laser power is 750 W, followed by the scanning speed, and finally, the powder feeding rate. The variation in the powder feed rate does not have a significant impact on the mean width value. Additionally, there is minimal change in the width at powder feed rates of 2.1 g/min, 4.33 g/min, and 6.67 g/min. From the interaction plots, it can be seen that there is no interaction between the laser power and scanning speed, or between the laser power and powder feeding rate. On the contrary, when the scanning speed is 9 mm/s and the powder feeding rate is 11 mm/s, and the powder feeding rate is 2.1 g/min and 4.33 g/min, the response quantity changes differently at different levels of the other parameter. This indicates that there is a clear interaction between these two factors.

3.3.3. Influence of Process Parameters on Wetting Angles of the Depositions

The wetting angle is one of the most crucial parameters for assessing the uniformity of the deposited layer, and a wetting angle of less than 120° results in an inadequate formation.

From Table 12, the F value of the model is 6.99, with a p value < 0.0001, indicating that the model is statistically significant. The regression coefficients indicate that the laser power, scanning speed, powder feed rate, and their interaction collectively explain 91.06%

of the variation in the wetting angle. The comparison with the mean square of the other parameters yielded a low standard error, indicating that the model is satisfactory. From the *p* value results, it is clear that the *p* values of the scanning speed and powder feeding rate are both less than 0.05. Therefore, statistically, these two factors have a significant effect on the wetting angle results. The *p* value for the laser power and the interaction between two of the three factors is greater than 0.05. Therefore, none of their effects on the wetting angle are statistically significant. The sum of the squares values of the individual factors in the ANOVA table were used to determine the effect ratio of each influencing factor on the wetting angle. Pie charts depicting the practical significant factors were constructed, as shown in Figure 15a, and Pareto charts are shown in Figure 15b.

Table 12. Results of variance analysis of wetting angles of the depositions.

Source	DF	Adj SS	Adj MS	F	*p*
Mold	35	14,048.8	401.40	6.99	0.000
Biometrics	9	12,120.5	1346.73	23.44	0.000
Laser power	4	169.3	42.32	0.74	0.576
Scanning speed	3	4040.3	1346.77	23.44	0.000
Powder feeding rate	2	7911.0	3955.48	68.84	0.000
2 Factor interactions	26	1928.3	74.17	1.29	0.266
Laser power * Scanning speed	12	920.9	76.74	1.34	0.263
Laser power * Powder feeding rate	8	318.2	39.77	0.69	0.695
Scanning speed * Powder feeding rate	6	689.2	114.87	2.00	0.105
Error	24	1379.0	57.46		
Total	59	15,427.9			

S = 7.58023; R-sq = 91.06%; R-sq (Adj) = 78.03%; R-sq (Pre) = 44.13%.

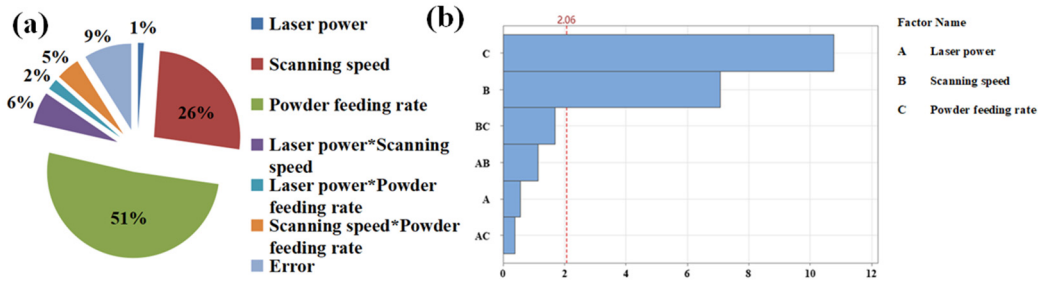


Figure 15. (**a**) Pie chart of practical significance factor of wetting angle of the depositions. (**b**) Pareto diagram in response to a wetting angle θ/° normalization effect.

From Figure 15a, it can be seen that the powder feeding rate has a significant effect on the wetting angle, accounting for 51% of the variation in the wetting angle. This indicates that the powder feeding rate is the most influential factor in determining the wetting angle. The scanning speed is the second most important factor, accounting for 26%. Of all the factors, only 1% of the variation is attributed to the laser power. The Pareto chart also demonstrates that the powder feeding rate and scanning speed are the most influential factors affecting the wetting angle.

The main effect plots and interaction plots of the studied parameters on the wetting angle are shown in Figures 16 and 17, respectively.

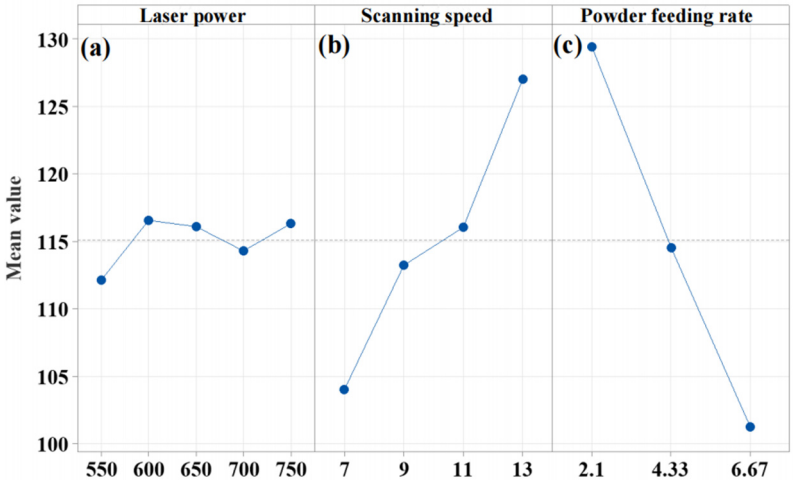


Figure 16. The response is a wetting angle θ/° main effect diagram. (**a**) Laser power. (**b**) Scanning speed. (**c**) Powder feeding rate.

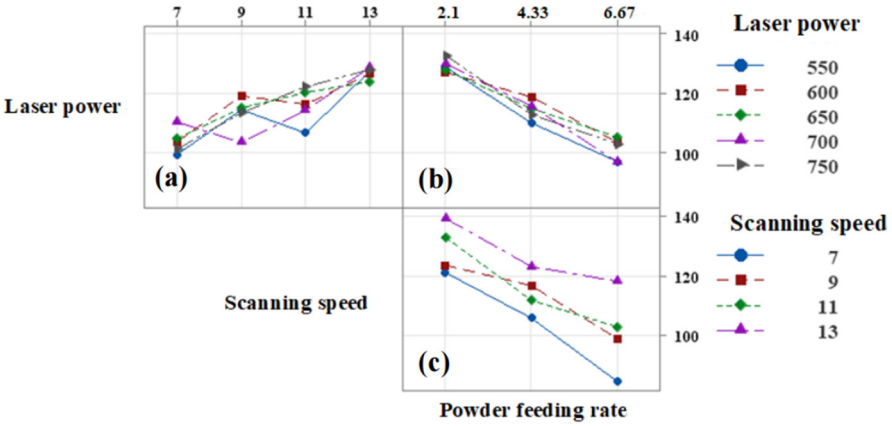


Figure 17. The response is a wetting angle θ/° interaction graph. (**a**) Laser power and scanning speed. (**b**) Laser power and powder feeding rate. (**c**) Scanning speed and powder feeding rate.

As shown in Figure 16, the wetting angle of the deposited layer is most affected when the laser power is 600 W, the scanning speed is 13 mm/s, and the powder feeding rate is 2.1 g/min. The effect on the wetting angle is significantly greater than the mean value when the powder feeding rate is 2.1 g/min, followed by the scanning speed, and finally, the laser power. The change in laser power does not have a significant effect on the mean value of the wetting angle, and there is almost no noticeable change in the wetting angle from 550 W to 750 W. However, the impact of laser power on the wetting angle is still considerable. From the interaction plot, it can be seen that there is no significant effect of two-by-two interactions among the three factors. Additionally, with different parameter values, the wetting angle shows a consistent change trend.

The results of the residual plots for the height, width, and wetting angle of the sedimentary layer are presented alongside the analysis of variance (ANOVA) results. Additionally, pie charts depicting the significant influences, Pareto charts, main effect plots, and interaction plots are included. These are given to ensure the validity of the results by strictly adhering to the assumptions of homogeneity of variance and normality of residuals. As depicted in Figure 18, the analysis of the height, width, and wetting angle of the 60 groups of sedimentary layers reveals a close approximation to a straight line. This suggests that the assumption of normality is satisfied, indicating a strong fit for the model.

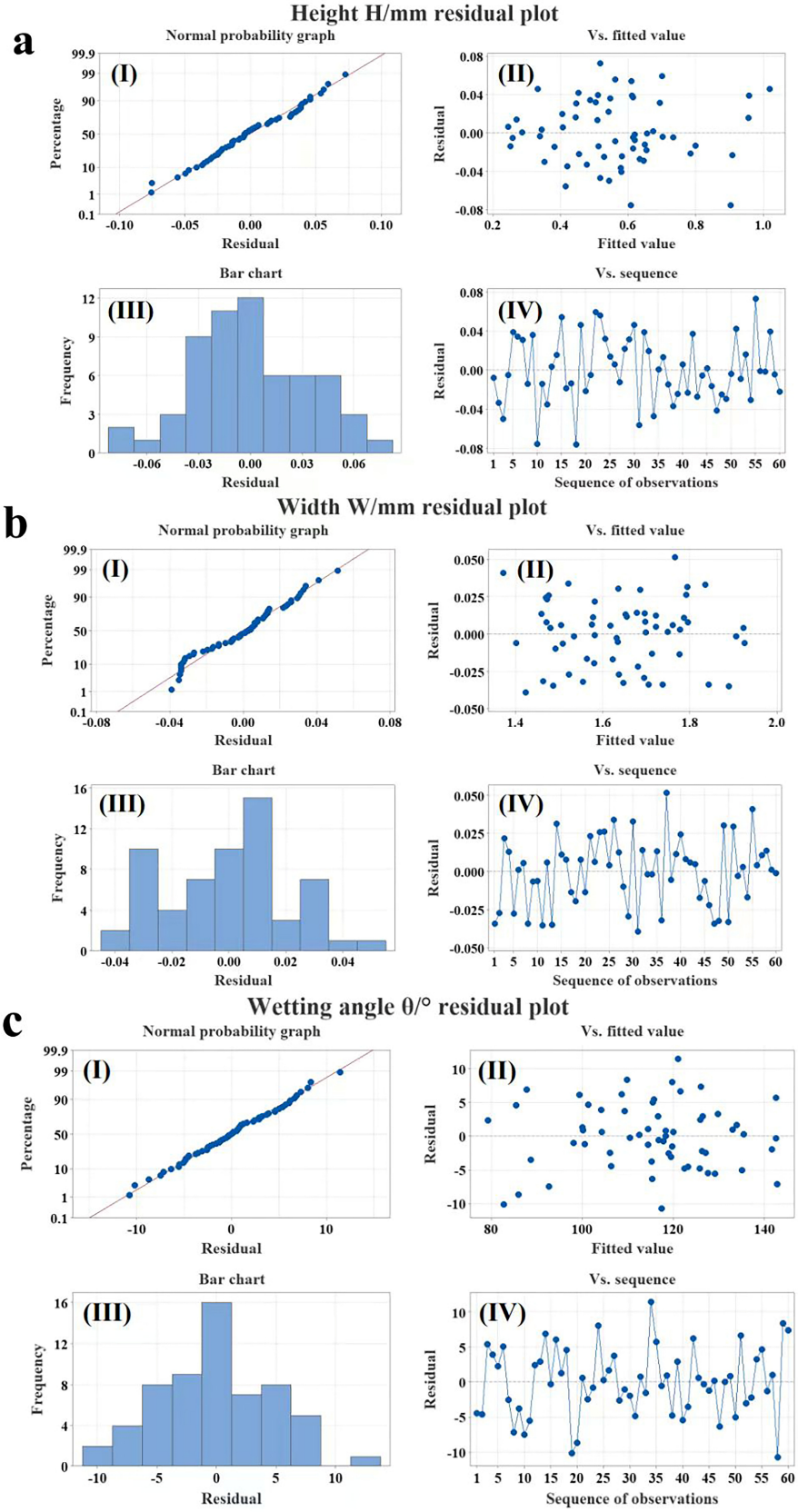


Figure 18. (**a**) Height H/mm residual plot. (**b**) Width W/mm residual plot. (**c**) Wetting angle θ/° residual plot.

A laser power of 600~750 W, scanning speeds of 9 mm/s and 11 mm/s, and a powder feeding rate of 6.67 g/min were selected to laser additively fabricate a single multi-layer,

multi-channel deposition layer. In this case, the aspect ratio ranged from 0.4 to 0.5, and the wetting angle was less than 120°. As shown in Figure 19a, the cross-sectional morphology of the single-pass, multi-layer deposited layer exhibits a porous and pronounced steepening phenomenon. The wetting angle gradually decreases, and there are noticeable inclusions within the deposited layer, which will adversely affect the mechanical properties. On the contrary, Figure 19b shows that six sets of single multi-layer, multi-channel deposited layers were fabricated using direct laser deposition, with a laser power of 550 W~750 W, scanning speeds of 9 mm/s and 13 mm/s, and powder feeding rates of 2.1 g/min and 4.33 g/min. The aspect ratios ranged from 0.2 to 0.3, and the wetting angles were greater than 120°. The cross-sectional morphology of group (b) shows that the surface of the deposited layers in this value range is smooth, and the defects, such as porosity and inclusions, are significantly reduced.

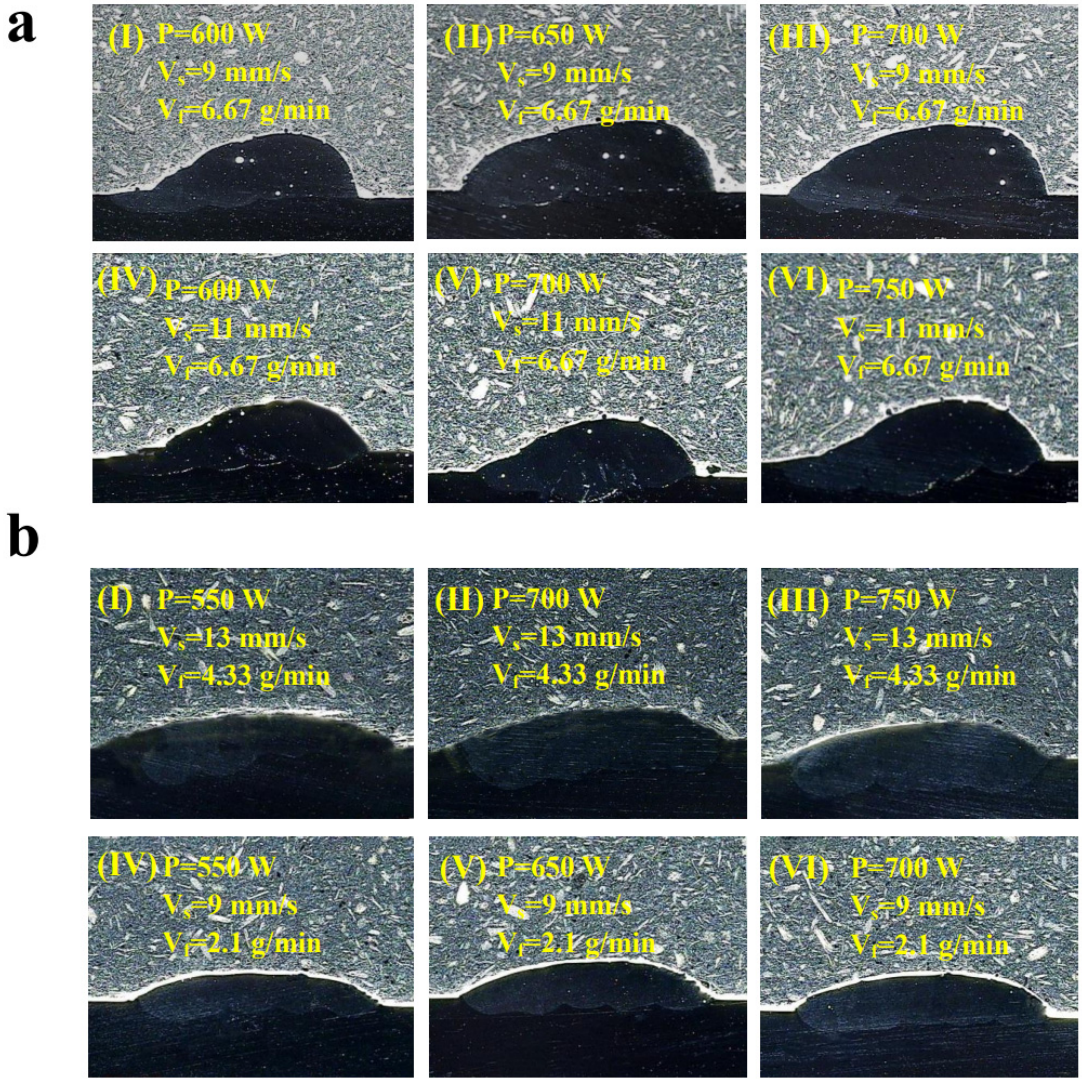


Figure 19. (**a**) Cross-sectional topography of direct laser deposition single-layer, multi-channel intercalation. (**b**) Morphology of a single-layer, multi-pass, non-inclusion cross-section for direct laser deposition.

4. Theoretical Deduction

Wettability is an important property of a material surface, and the degree of wetting is commonly measured using the wetting angle θ [22]. Young's equation describes the relationship between the contact angle and the three interfacial tensions [23]. Young's equation, also known as the wetting equation, holds a significant position in the field

of material surface interfaces. It serves as the foundation for quantifying the surface wettability of a material [22] and calculating the surface tension of a solid material using the wetting angle [24]. As the research progressed, it was found that Young's equation needed to be corrected by introducing line tension when the droplets are small [25]. The cross-section of a single-pass coating exhibits morphological similarities to the lying drop and spherical crown models. Therefore, deriving a mathematical model of the relationship between the geometrical parameters of the deposited layer by combining surface tension and gravity requires the assistance of Young's equation, which is based on the laying drop and crown models.

Here, it is important to emphasize that the spherical crown model is solely a theoretical derivation of the cross-section parameter relationships for a single layer with a more regular single-channel cross-section morphology profile. Some irregular cross-sectional morphologies appear in Figures 3 and 4. These irregular morphologies indicate that this parameter combination is not within the optimal range, and this particular parameter is not applicable to the theoretical derivation of the ball-and-crown model.

The model the crown of the sphere, as shown in Figure 20, is based on the formula for the area of a circle:

$$S = \pi r^2 \tag{1}$$

The formula for calculating the volume of a spherical crown is:

$$V = \pi h^2 R - \pi h^3/3 \tag{2}$$

And the other geometric relationships:

$$(R - h)^2 + r^2 = R^2 \tag{3}$$

The associations (1)–(3):

$$V = 1/6\pi h\left(h^2 + 3r^2\right) = 1/6\pi h^3 + 1/2hS \tag{4}$$

Therefore, the crown height h, volume V, and contact area S satisfy the equation:

$$h^3 + 3Sh/\pi - 6V/\pi = 0 \tag{5}$$

Equation (5) is a cubic equation, which has a unique real root determined by solving for the roots of a cubic equation in one variable:

$$h = \sqrt[3]{\frac{3V}{\pi} + \sqrt{\frac{9V^2}{\pi^2} + \frac{S^3}{\pi^3}}} + \sqrt[3]{\frac{3V}{\pi} - \sqrt{\frac{9V^2}{\pi^2} + \frac{S^3}{\pi^3}}} \tag{6}$$

And

$$R = 1/2(h + S/\pi h) \tag{7}$$

$$\theta = \arccos(1 - h/R) \tag{8}$$

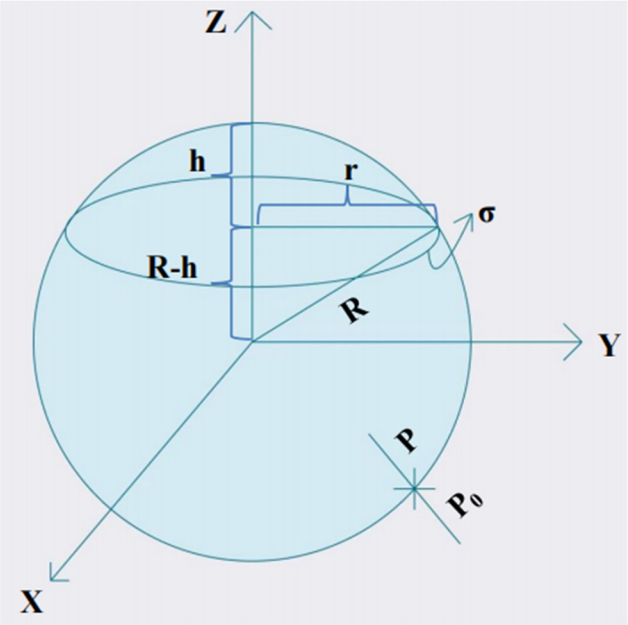


Figure 20. Spherical crown model.

The relationship between the crown height h, crown volume V, and contact area S, as well as the wetting angle θ and crown height h, is determined using the crown model.

However, in reality, the deposited layer's surface will assume a spherical shape due to surface tension, as illustrated in Figure 20. This occurs when the tension per unit length of the spherical shell is set to σ, the *Z* axis serves as the axis of symmetry, and there is a difference in air pressure between the inside and outside of the spherical crown, which is denoted as ΔF.

$$\Delta F = \int_0^{2\pi} d\sigma \int_0^{\alpha} (P - P_0)\cos\theta R^2 \sin\theta d\theta = \pi(P - P_0)R^2\sin^2\alpha \quad (9)$$

Once the spherical shell is in equilibrium, the difference between the internal and external pressures, ΔF, must be cancelled out by the surface tension of the shell, as shown in Figure 20.

$$\Sigma = \sigma \cdot \sin\alpha \cdot 2\pi R \sin\alpha \quad (10)$$

And

$$\Delta F = \Sigma \quad (11)$$

So

$$\pi(P - P_0)R^2\sin^2\alpha = \sigma \cdot \sin\alpha \cdot 2\pi R \sin\alpha \quad (12)$$

This can be introduced as

$$\sigma = \frac{(P - P_0)R}{2}, \; R = \frac{2\sigma}{(P - P_0)} \quad (13)$$

Combining (8) with (13),

$$\theta = \arccos[1 - \frac{h(P - P_0)}{2\sigma}] \quad (14)$$

The relationship between the wetting angle θ, crown height h, internal and external pressures P and P_0, and line tension σ was determined by solving the crown model in conjunction with the surface tension.

The surface wettability of a material is influenced by three factors: the physicochemical properties of the material itself, surface tension, and gravity. A previous spherical crown

model has taken into account the effect of surface tension, but it has not considered the influence of gravity on shape. When considering the effect of gravity, the analysis of the spherical crown model is performed in conjunction with Young's equation, which is also known as the wetting equation.

As shown in Figure 21, the relationship between the wetting angle θ and the interfacial tension is described by Young's equation, proposed by T. Young through mechanical analysis, i.e.,

$$\gamma_{lv}\cos\theta = \gamma_{sv} - \gamma_{sl} \quad (15)$$

where γ_{sv} represents the solid surface tension, γ_{lv} represents the liquid surface tension, and γ_{sl} represents the solid–liquid interfacial tension. Some studies [21] have explored the relationship between gravity and the wetting angle. However, further analyses were carried out based on the schematic of the spherical crown model, in conjunction with the previously described surface tension. A small section of the rectangle ABCD is intercepted from the edge of the spherical crown, as shown in Figure 22.

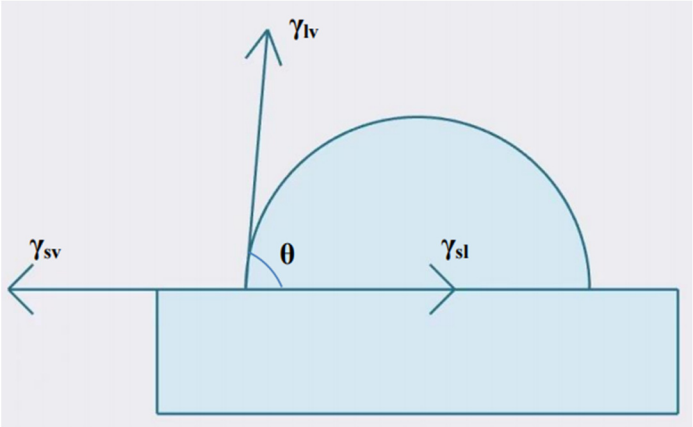


Figure 21. Schematic diagram of T. Young's equation.

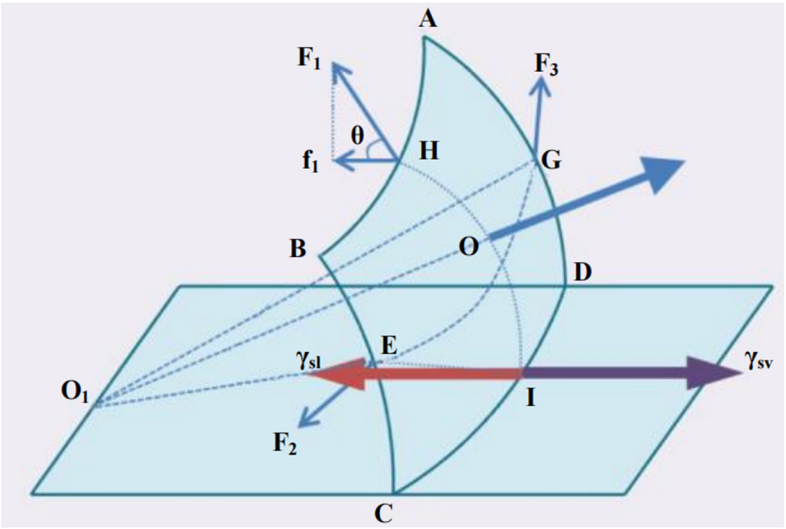


Figure 22. Tiny rectangle at the edge of the crown.

Combining Figures 21 and 22 shows that the side AB of the small rectangle ABCD is affected by surface tension:

$$F_1 = \gamma_{lv} \cdot AB \quad (16)$$

The component force in the horizontal direction:

$$f_1 = \gamma_{lv} \cdot AB \cdot \cos\theta \tag{17}$$

Similarly, sides BC and AD are subject to surface tension:

$$F_2 = \gamma_{lv} \cdot BC,\ F_3 = \gamma_{lv} \cdot AD \tag{18}$$

The component force in the horizontal direction:

$$f_2 = \gamma_{lv} \cdot BC \cdot \cos\theta, f_3 = \gamma_{lv} \cdot AD \cdot \cos\theta \tag{19}$$

The surface tension on the edge CD:

$$f_4 = \gamma_{sl} \cdot CD - \gamma_{sv} \cdot CD \tag{20}$$

Consider the case under a gravitational field and let the height of the droplet be denoted as h. The rectangle ABCD is subjected to pressure from the droplet in the direction of OO_1. The magnitude of this pressure is determined by the relationship between the force, pressure, and area:

$$F_5 = P \cdot S = \rho gh \cdot AB \cdot BC \tag{21}$$

The component force in the horizontal direction:

$$f_5 = \rho gh \cdot AB \cdot BC \cdot \sin\theta \tag{22}$$

The reason for this is that the magnitude of the combined force in the horizontal direction is zero:

$$f_6 = f_1 + f_2 + f_3 + f_4 + f_5 \tag{23}$$

$$\gamma_{lv} \cdot AB \cdot \cos\theta + \gamma_{lv} \cdot BC \cdot \cos\theta + \gamma_{lv} \cdot AD \cdot \cos\theta + \gamma_{sl} \cdot CD - \gamma_{sv} \cdot CD - \rho gh \cdot AB \cdot BC \cdot \sin\theta = 0 \tag{24}$$

The formula tidied up is as follows:

$$\gamma_{sv} \cdot CD = \gamma_{lv} \cdot AB \cdot \cos\theta + \gamma_{lv} \cdot BC \cdot \cos\theta + \gamma_{lv} \cdot AD \cdot \cos\theta + \gamma_{sl} \cdot CD - \rho gh \cdot AB \cdot BC \cdot \sin\theta \tag{25}$$

As can be seen in Figure 20,

$$AB = CD,\ BC = AD \tag{26}$$

$$\gamma_{sv} = \gamma_{lv} \cdot \cos\theta + 2 \cdot \gamma_{lv} \cdot \frac{BC \cdot \cos\theta}{CD} + \gamma_{sl} - \rho gh \cdot BC \cdot \sin\theta \tag{27}$$

Let BC = l:

$$\gamma_{sv} = \gamma_{lv} \cdot \cos\theta + 2 \cdot \gamma_{lv} \cdot \frac{l \cdot \cos\theta}{CD} + \gamma_{sl} - \rho gh \cdot l \cdot \sin\theta \tag{28}$$

From the relationship between the line tension σ and l, γ_{lv}, let $\gamma_{lv} \cdot l = \sigma$, then the equation can be written as

$$\gamma_{sv} = \gamma_{lv} \cdot \cos\theta + 2 \cdot \frac{\sigma \cdot \cos\theta}{CD} + \gamma_{sl} - \rho gh \cdot l \cdot \sin\theta \tag{29}$$

When the droplets are small and the height of the droplet is negligible, there is

$$\gamma_{sv} = \gamma_{lv} \cdot \cos\theta + 2 \cdot \frac{\sigma \cdot \cos\theta}{CD} + \gamma_{sl} \tag{30}$$

When the droplets are large and the line tension is negligible, there is

$$\gamma_{sv} = \gamma_{lv} \cdot \cos\theta + \gamma_{sl} - \rho g h \cdot l \cdot \sin\theta \tag{31}$$

Combining the relationship between the wetting angle θ, the crown height h, the internal and external pressures P and P_0, and the line tension σ, which was derived earlier based on the spherical crown model combined with the surface tension solution, and substituting it into the above equation, it can be expressed as

$$\gamma_{sv} = \gamma_{lv} \cdot [1 - \frac{h(P - P_0)}{2\sigma}] + \frac{2\sigma - h(P - P_0)}{CD} + \gamma_{sl} - \rho g h \cdot l \cdot \sin\theta \tag{32}$$

In conjunction with (15), there is

$$\tan\theta = \frac{1}{h} \cdot \frac{2\gamma_{lv}}{CD\rho g} \tag{33}$$

The novelty of this study is demonstrated by the combination of cross-sectional morphology diagrams and previously obtained data for 60 sets of process parameter combinations, in conjunction with Equation (33). The parameter values can fluctuate within different environments. When CD, ρ, g, and γ_{lv} in Equation (33) are determined, there exists a quantitative relationship between the height of the sedimentary layer h and the wetting angle θ. Based on this relationship, a set of h and θ can be determined by selecting the process parameters before conducting an experiment or engineering project. This allows us to assess whether the selected set of process parameters can produce a single-layer, single-pass morphology that meets the requirements of the latter. By selecting fewer consumables and ensuring high-level efficiency, the suitability of the process parameters can be determined to the greatest extent possible, and the wear can be minimized.

5. Conclusions

The research in this paper combines experiments and a theory. This combination aims to illustrate the relationship between the geometrical shape parameters of the single-layer, single-pass cross-section of direct laser deposition. The combination of experimentation and a theory provides a more comprehensive understanding of the relationship between the variation of cross-section parameters in layers deposited via direct laser deposition. The theory is utilized to explain the phenomenon, while the experiment serves to validate the findings. Based on this, it can be deduced that in the future, the practical application of engineering will greatly benefit from the direct laser deposition of sedimentary layer cross-section geometry. This deduction is supported by the theoretical derivation of the formula illustration. By combining these process parameters, it is expected that the efficiency and cost savings will be significantly improved. In the shortest possible time, the minimum amount of material can be verified to determine whether to proceed with the process parameters of this parameter group. This can significantly enhance industrial efficiency and save costs. This can greatly improve industrial efficiency. The conclusions of this paper are presented in the following four points:

(1) The laser power, scanning speed, and powder feeding rate have varying degrees of influence on the macroscopic forming morphology of the single-pass direct laser deposition of Inconel 738 powders. The laser power has a significant effect on the width (W) and a smaller effect on the height-to-width ratio (H/W). The scanning speed has a moderate effect on the height (H), width (W), and wetting angle (θ). The powder feeding rate has a very significant effect on the height (H) and wetting angle (θ), but it does not have a significant effect on the width (W). The laser power and scanning speed have different effects on the overall shape of the single-pass laser additive manufacturing of Inconel 738 powders.

(2) Laser power is the most important factor affecting W. As the laser power increases, W gradually increases. The scanning speed and powder feeding rate are the main factors

that influence H. As the scanning speed increases, H gradually decreases. Conversely, as the powder feeding rate increases, H gradually increases. The powder feeding rate is the most influential factor in θ. With the increase in powder feeding rate, θ gradually decreases.

(3) On the basis of Young's equation, the surface tension term and gravity term are included, indicating that the wetting angle of the material surface is influenced not only by the three interfacial tensions, but also by the surface tension and gravity. Based on surface tension and gravity, the functional relationship between H and θ is established. This relationship can be used to develop the theory of process analysis and guide the implementation of the process. It can also be used to predict and evaluate the trend and quality of deposition changes.

(4) From the experimental results, it can be seen that the single layer with multiple depositions obtained has the fewest defects and inclusions as well as a higher efficiency when the H/W value is between 0.2 and 0.3 and θ is greater than 120°. At this time, the range of laser power is 550–750 W, the range of scanning speed is 7–13 mm/s, and the range of powder feeding rate is 2.1–4.33 g/min.

Author Contributions: Conceptualization, K.Q. and C.Q.; methodology, K.Q. and P.C.; software, K.Q. and W.W.; validation, K.Q., P.C. and H.L.; formal analysis, K.Q. and C.Q.; investigation, K.Q.; resources, K.Q. and C.Q.; data curation, K.Q.; writing—original draft preparation, K.Q.; writing—review and editing, K.Q.; visualization, K.Q. and C.Q.; supervision, K.Q. and C.Q.; project administration, K.Q., W.W. and C.Q.; funding acquisition, C.Q. All authors have read and agreed to the published version of the manuscript.

Funding: This project was supported by National Natural Science Foundation of China (Grant No. 52371032).

Institutional Review Board Statement: Not applicable.

Informed Consent Statement: Not applicable.

Data Availability Statement: Data are contained within the article.

Conflicts of Interest: The authors declare no conflict of interest.

References

1. Ren, G.; Guo, S.; Zhang, B. Surface Integrity of Inconel 738LC Parts Manufactured by Selective Laser Melting Followed by High-speed Milling. *Chin. J. Mech. Eng.* **2023**, *36*, 81–95. [CrossRef]
2. Jie, H. Effect of laser power on the densification of selected zone laser melting of IN738LC alloy. *Mater. Guide* **2022**, *36*, 426–429.
3. Kastner, C.; Neugebauer, M.; Schricker, K.; Bergmann, J.P. Strategies for increasing the productivity of pulsed laser cladding of hot-crack susceptible nickel-base superalloy Inconel 738 LC. *J. Manuf. Mater. Process.* **2020**, *4*, 84. [CrossRef]
4. Taheri, M. Analysis of Solidification and Liquation Cracks in the Electron Beam Welding of IN738 Superalloy. *Metallogr. Microstruct. Anal.* **2021**, *10*, 815. [CrossRef]
5. Mostafa, A.; Masoumeh, K. Direct metal deposition of IN625 on IN738LC superalloy: Microstructure and crack analysis. *Appl. Phys. A* **2021**, *127*, 305.
6. Ponnusamy, P.; Rahman, R.A.; Masood, S.H.; Ruan, D.; Palanisamy, S. Mechanical properties of SIM-printed aluminum alloys: A review. *Materials* **2020**, *13*, 4301. [CrossRef]
7. Cheng, J.; Xing, Y.H.; Dong, B.; Zhao, L.J.; Liu, H.N.; Chang, T.Y.; Chen, M.J.; Wang, J.H.; Lu, J.W.; Wan, J. An overview of laser metal deposition for cladding: Defect formation mechanisms, defect suppression methods and performance improvements of laser-cladded layers. *Materials* **2022**, *15*, 5522. [CrossRef]
8. Zhang, Q.; Tong, W.; Chen, Z.; Yao, J.; Li, Z.; Feng, K.; Kovalenko, V.S. Influence of spot size on the geometrical characteristics of laser deep quenching hardened layer of 42CrMo steel. *Surf. Technol.* **2020**, *49*, 254–261.
9. Bax, B.; Rajput, R.; Kellet, R.; Reisacher, M. Systematic evaluation of process parameter maps for laser cladding and direct energy deposition. *Addit. Manuf.* **2018**, *21*, 487–494.
10. Ren, D.; Lin, Q.; Li, T.; Qi, H. Research on laser cladding repair process and path of cold work mold surface. *Surf. Technol.* **2018**, *47*, 54–60.
11. Zhang, R.; Zhang, R.; Chen, Y.; Liu, G. Research on the process parameters of single-pass molding process for laser cladding of iron-based alloys. *Therm. Process. Technol.* **2017**, *46*, 162–165+169.
12. Pinkerton, A.J. Advances in the modeling of laser direct metal deposition. *J. Laser Appl.* **2014**, *27*, s15001. [CrossRef]

13. Perevoshchikova, N.; Rigaud, J.; Sha, Y.; Heilmaier, M.; Finnin, B.; Labelle, E.; Wu, X. Optimisation of selective laser melting parameters for the Ni-based superalloy IN738LC using Doehlert's design. *Rapid Prototyp. J.* **2017**, *23*, 881–892. [CrossRef]
14. Mondal, S.; Bandyopadhyay, A.; Pal, P.K. Application of artificial neural network for the prediction of laser cladding process characteristics at Taguchi–based optimized condition. *Int. J. Adv. Manuf. Technol.* **2014**, *70*, 2151–2158. [CrossRef]
15. Barekat, M.; Razavi, R.S.; Ghasemi, A. Nd: YAG laser cladding of Co-Cr-Mo alloy on y-TiAl substrate. *Opt. Laser Technol.* **2016**, *80*, 145–152. [CrossRef]
16. Ansari, M.; Shoja, R.R.; Barekat, M. An empirical-statistical model for coaxial laser cladding of NiCrAIY powder on Inconel 738 superalloy. *Opt. Laser Technol.* **2016**, *86*, 136–144. [CrossRef]
17. Muthuramalingam, T. Surface quality measures analysis and optimization on machining titaniumalloy using CO_2 based laser beam drilling process. *J. Manuf. Process.* **2021**, *62*, 1–6. [CrossRef]
18. Elsheikh, A.H. Improving laser cutting quality of polymethylmethacrylate sheet: Experimental investigation and optimization. *J. Mater. Res. Technol.* **2020**, *9*, 1325–1339. [CrossRef]
19. Khoshaim, A.B. Experimental investigation on laser cutting of PMMA sheets: Effects of process factors on kerf characteristics. *J. Mater. Res. Technol.* **2021**, *11*, 235–246. [CrossRef]
20. Elsheikh, A.H. Modeling of the Transient Temperature Field during Laser Heating. *Lasers Manuf. Mater. Process.* **2021**, *8*, 97–112. [CrossRef]
21. Elsheikh, A.H. Prediction of laser cutting parameters for polymethylmethacrylate sheets using random vector functional link network integrated with equilibrium optimizer. *J. Intell. Manuf.* **2020**, *32*, 1377–1388. [CrossRef]
22. Bormashenko, E. Progress in understanding wetting transitions on rough surfaces. *Adv. Colloid Interface Sci.* **2014**, *222*, 92–103. [CrossRef] [PubMed]
23. Young, T. An essay on the cohesion of fluids. *R. Soc. Lond. Philos. Trans.* **1805**, *95*, 65–87.
24. Tavana, H.; Neumann, A.W. Recent process in the determination of solid surface tensions from contact angles. *Adv. Colloid Interface Sci.* **2007**, *132*, 1–32. [CrossRef] [PubMed]
25. Liu, Y. Research on Surface Wettability of Materials Affected by Gravity. Ph.D. Thesis, Northwestern Polytechnical University, Xi'an, China, 2017.

Disclaimer/Publisher's Note: The statements, opinions and data contained in all publications are solely those of the individual author(s) and contributor(s) and not of MDPI and/or the editor(s). MDPI and/or the editor(s) disclaim responsibility for any injury to people or property resulting from any ideas, methods, instructions or products referred to in the content.